A modified constitutive model for tensile deformation of 9%Cr steel under prior fatigue loading

Wei Zhang [a,b,c], *Xiaowei Wang* [a,b,d,*], *Haofeng Chen* [c,*], *Tianyu Zhang* [a,b], *Jianming Gong* [a,b,*]

[a] *School of Mechanical and Power Engineering, Nanjing Tech University, Nanjing, 211816, China*

[b] *Jiangsu Key Lab of Design and Manufacture of Extreme Pressure Equipment, Nanjing, 211816, China*

[c] *Department of Mechanical and Aerospace Engineering, University of Strathclyde, Glasgow, G1 1XJ, UK*

[d] *Faculty of Engineering and Architecture, Ghent University, Zwijnaarde, B-9052, Belgium*

***Corresponding authors:**

E-mail: *xwwang@njtech.edu.cn (X. Wang); haofeng.chen@strath.ac.uk (H. Chen); gongjm@njtech.edu.cn (J. Gong)*

Tel.: +86 25 58139361; Fax: +86 25 58139361.

ABSTRACT

Reliable constitutive models are necessary for the precise design and manufacture of complicated components. This study is devoted to developing a modified constitutive model to capture the effects of prior fatigue loading on subsequent tensile deformation of 9%Cr steel. In the proposed model, a strain hardening rule combined with a defined fatigue damage parameter were introduced to represent prior fatigue damage. The defined fatigue damage parameter based on the inelastic strain range of each cycle is capable of describing the evolution of tensile strength, recovery of martensite laths and decline of dislocation density, regardless of the variation in fatigue loading conditions. To validate the predictive capacity of the proposed model, experimental tensile results at different strain amplitudes, lifetime fractions and hold times of prior fatigue loading were compared with the predicted results. Good agreement between experimental and predicted results indicates that the proposed model is robust in describing the tensile behaviour under prior

fatigue loading. Moreover, few determined material parameters are required, which makes the proposed model convenient for practical applications.

***Key words**:* 9%Cr steel; Prior fatigue loading; Constitutive model; Fatigue damage parameter

1. Introduction

From an engineering point of view, reliable constitutive models are necessary for the determination of the mechanical behaviour of materials, especially for the modern computer aided design (CAD) (Livatyali et al., 2001). Among these models, constitutive models for tensile deformation should first be considered, since they enable the determination of the yield stress, which is of crucial concern for the component design and manufacture. However, tensile properties can be altered by in-service loadings, particularly the low cycle fatigue (LCF) and creep fatigue interaction (C-F) loadings (Sánchez-Santana et al., 2008; Sánchez-Santana et al., 2009; Moćko et al., 2014; Moćko et al., 2015; Moćko et al., 2016; Mariappan et al., 2015; Mariappan et al., 2016; Mariappan et al., 2017). Such complicated loading conditions may result in premature failure if the component design depends only on the original state. Over the past several years, intensive experimental investigations have been conducted to evaluate the remnant tensile resistance under prior fatigue loading (Sánchez-Santana et al., 2008; Moćko et al., 2016; Mariappan et al., 2017; Paul et al., 2010; Paul et al., 2011; Hamdoon et al., 2011). It has been revealed that the effect of prior fatigue loading on remnant tensile properties depends on both loading and material types, e.g., for 304LN (Paul et al., 2010; Paul et al., 2011), 316L (Mariappan et al., 2015; Mariappan et al., 2016), AISI 1022 (Hamdoon et al., 2011) and TiAl6V4 (Moćko et al., 2014) alloys, the prior fatigue loading slightly strengthened the remnant tensile strength, whereas for AISI 4140-T (Sánchez-Santana et al., 2008; Sánchez-Santana et al., 2009) and 9%Cr (Mariappan et al., 2015; Mariappan et al., 2017) steels, the prior fatigue loading degraded the subsequent tensile properties. Microstructural analysis illustrates that the evolution of remnant tensile properties of stainless

steel is mainly attributed to the alternation of dislocation density and subgrain size during the prior fatigue process (Mariappan et al., 2015; Paul et al., 2010). Moćko et al. further pointed out that prior fatigue loading induced voids and micro-cracks at the grain boundary of DP 500 steel, which may contribute to the degradation of remnant tensile resistance (Moćko et al., 2016). In addition, our previous work revealed that outer surface oxidation formed during hold process of C-F loading, introducing additional damage on remnant tensile elongation of 9%Cr steel (Zhang et al., 2019). Nevertheless, related studies on effective modelling approaches for the prediction of remnant tensile deformation are still limited.

To date, a great deal of effort has been devoted to develop numerous constitutive models to predict the tensile deformation behaviour of as-received materials under various loading conditions, such as different strain rates and different temperatures (Johnson et al., 1985; Zerilli et al., 1987; Khan et al., 1992; Meyers et al., 1994; Nemat-Nasser et al., 1998; Preston et al., 2003). Generally, these models can be classified into two categories: physically based models and empirical models. Physically based constitutive models can simulate tensile deformation of material accurately. However, physically based constitutive models are not always preferred due to the difficulty of determining the model constants (Lin et al., 2011). Empirical constitutive models, especially the Johnson-Cook (JC) model (Johnson et al., 1985), are usually adopted due to their convenience. However, to the best of the authors' knowledge, regarding the constitutive models under prior fatigue loading, the constitutive model developed by Moćko et al. (Moćko et al., 2016; Moćko et al., 2017) is the only existing model for capturing the prior fatigue loading effects. Nevertheless, in Moćko's work, the prior fatigue test is conducted under stress control and Moćko's model requires a large number of determined parameters. Moreover, in Moćko's study, the prior fatigue tests were performed at room temperature, while the prior fatigue tests of 9%Cr steel in the present work were conducted at 923 K under strain control.

Therefore, the constitutive model for tensile deformation of 9%Cr steel under strain-controlled prior fatigue loading and high temperature still needs intensive study.

In the current study, a modified constitutive model is developed to capture the effects of prior fatigue loading on subsequent tensile deformation of 9%Cr steel based on the original JC model. To account for the prior fatigue loading effects, a strain hardening rule combined with a defined fatigue damage parameter are introduced into the JC model. Experimental tensile results at different strain amplitudes, lifetime fractions and hold times of prior fatigue loading are used to verify the accuracy and capability of the proposed model. The parameter sensitivity analysis is also performed. Predicted results between the original JC model, Moćko's model and the proposed model are further compared to show the advantage of the proposed model.

2. Experimental methodology

2.1. Experimental procedures

The experiments conducted in the present study aim to evaluate the accuracy and the capacity of the proposed model. However, to avoid a repeated description of experimental methodology that has been elaborately depicted in our previous works (Wang et al., 2019; Zhang et al., 2019), only the main experimental methods and results are presented in the current study. The experimental procedures are schematically shown in Fig. 1, which includes fatigue lifetime determination test (Fig. 1(a)), prior fatigue test and subsequent tensile test (Fig. 1(c)). During the fatigue process, the strain-stress hysteresis loop (Fig. 1(b)) was recorded to obtain the inelastic strain range at each cycle, which will be used as the pivotal parameter to assess the fatigue damage. The material utilized in the experiments was P92 steel. Cylindrical specimens with 25 mm gauge length and 8 mm gauge diameter were machined from a pipe along the axial direction, as shown in Fig. 2. Specimens used for the fatigue test and the following tensile test all have the same geometrical dimensions. All tests were performed at 923 K by using the SINOTEST EQUIPMENT RPL100

test machine, which was equipped with a resistance heating furnace and the temperature was controlled within ±2 K. Fatigue tests were conducted in accordance with the ASTM E2714 standard (ASTM standard E2714, 2014). Tensile tests were conducted according to the ASTM E8 standard (ASTM Standard E8, 2004). Strain amplitudes of 0.25%, 0.4% and 0.6% were imposed on LCF tests. Tensile hold times ranging from 0 s to 600 s at 0.4% strain amplitude were imposed on C-F tests. Both the LCF and C-F tests were carried out under total strain control with a constant strain rate of 1×10^{-3} s^{-1}. Subsequent tensile tests were performed at the same strain rate. Detailed test data are summarized and listed in Table 1.

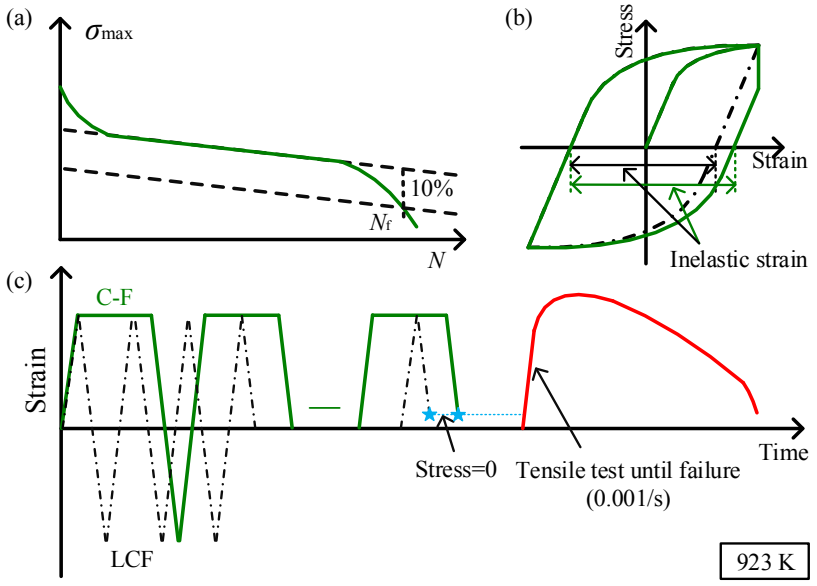

Fig. 1. Schematic representation of experimental procedures: (a) fatigue lifetime determination, (b) strain-stress hysteresis loops of LCF and C-F tests, (c) prior fatigue and subsequent tensile tests

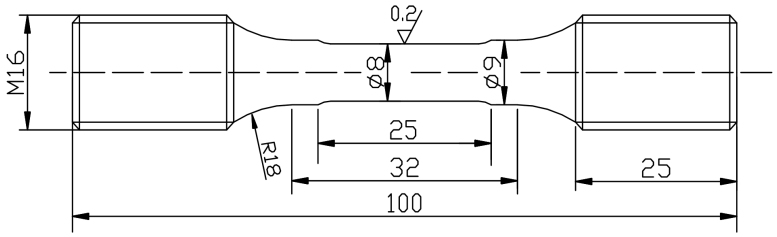

Fig. 2. Specimen geometry for fatigue followed by tensile test (unit: mm)

Table 1 Test conditions and results of prior fatigue loading and subsequent tensile testing data at 923 K

Test No.	Load pattern	Strain amplitude (%)	Hold time (s)	Lifetime fraction	Defined damage	Yield stress (MPa)	Ultimate tensile stress (MPa)	Martensite lath width (μm)	Dislocation density (m^{-2}) (Barrett et al., 2017)
1		As-received state			0	318	338	0.375	1.60×10^{14}
2	LCF	0.25	/	20%	0.58	258	278	0.580	1.13×10^{14}
3	LCF	0.25	/	50%	0.75	244	272	0.900	1.09×10^{14}
4	LCF	0.25	/	70%	0.76	233	260	1.200	1.07×10^{14}
5	LCF	0.4	/	20%	0.73	252	272	0.766	1.09×10^{14}
6	LCF	0.4	/	50%	0.82	230	251	1.100	1.04×10^{14}
7	LCF	0.4	/	70%	0.92	221	250	1.250	1.02×10^{14}
8	LCF	0.6	/	20%	0.74	240	257	/	/
9	LCF	0.6	/	50%	0.93	221	548	/	/
10	C-F	0.4	30	20%	0.73	246	267	0.755	1.19×10^{14}
11	C-F	0.4	180	20%	0.78	236	261	0.660	1.17×10^{14}
12	C-F	0.4	600	20%	0.72	234	268	0.775	1.14×10^{14}

2.2. Experimental results

Experimental observations have demonstrated that the remnant tensile properties of P92 steel are reduced by prior fatigue loading and the reduction level is related to lifetime fraction, strain amplitude and hold time (Wang et al., 2019; Zhang et al., 2019), as typically presented in Fig. 3 (engineering tensile curves). Mechanical properties (yield stress and ultimate tensile stress) determined from the engineering tensile curves are summarized in Table 1. The true stress-strain curves before the occurrence of necking are also depicted in Fig. 4. The true stress and true strain were calculated by Eqs. (1) and (2).

$$\sigma_T=\sigma_E(1+\varepsilon_E) \quad (1)$$

$$\varepsilon_T=\ln(1+\varepsilon_E) \quad (2)$$

where σ_T is true stress, ε_T is true strain, σ_E is engineering stress and ε_E is engineering strain. The as-received P92 steel presents obvious strain hardening behaviour at the initial stage of tensile process. Nevertheless, the evident strain hardening behaviour was weakened by the prior fatigue loading, as shown in Fig. 4. The

decline in dislocation density during prior fatigue process was mainly responsible for the phenomenon (Wang et al., 2019). Due to the reduction of dislocation density after prior fatigue loading, the dislocation strengthening is decreased, and therefore the resistance of the material to deformation decreased. As a result, weakened strain hardening was observed. Moreover, higher lifetime fraction and strain amplitude of prior fatigue loading led to the lower flow stress, and more evident deterioration of the remnant tensile properties. However, the tensile curves after different hold times almost overlap with each other which indicated the increase in hold time hardly altered the remnant tensile properties. All these observed phenomena will be quantified by the defined fatigue damage parameter and will be captured by the proposed model.

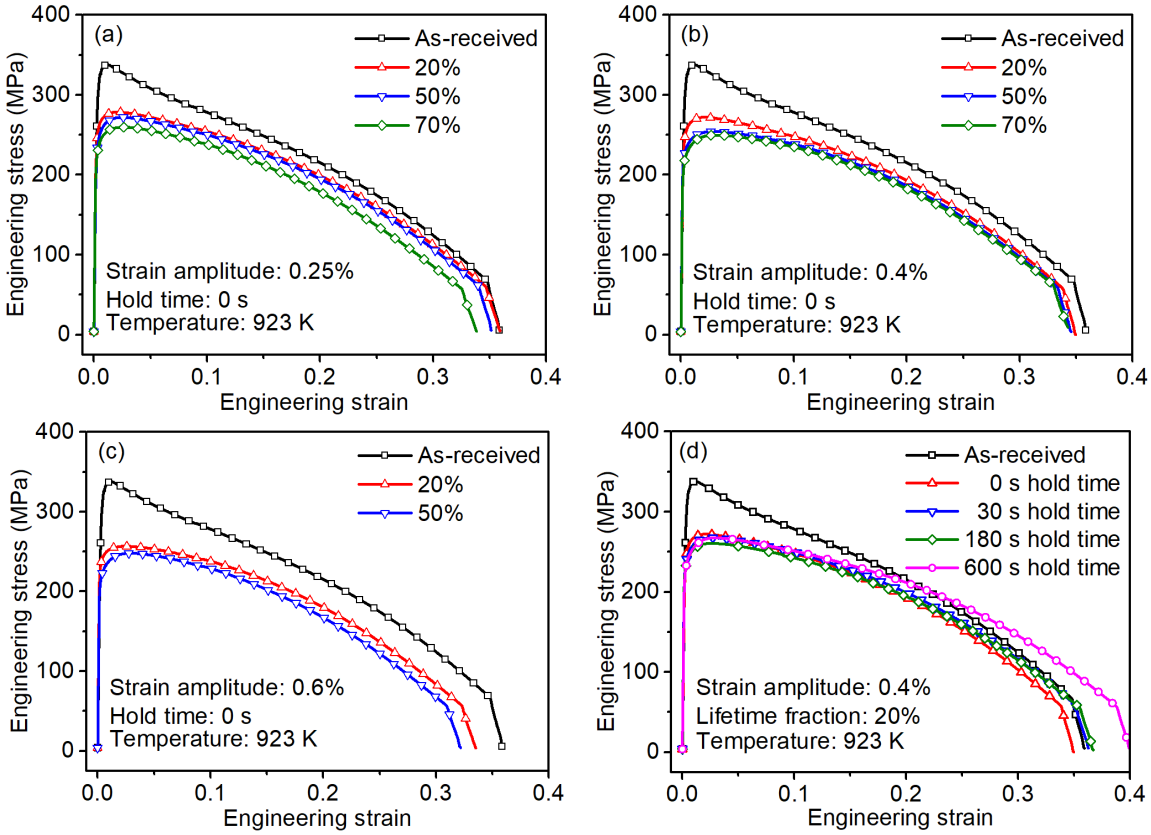

Fig. 3. Engineering tensile curves after various prior fatigue loading conditions: (a) 0.25% strain amplitude prior LCF loading, (b) 0.4% strain amplitude prior LCF loading, (c) 0.6% strain amplitude prior LCF loading, (d) 20% lifetime fraction prior C-F loading (Wang et al., 2019; Zhang et al., 2019)

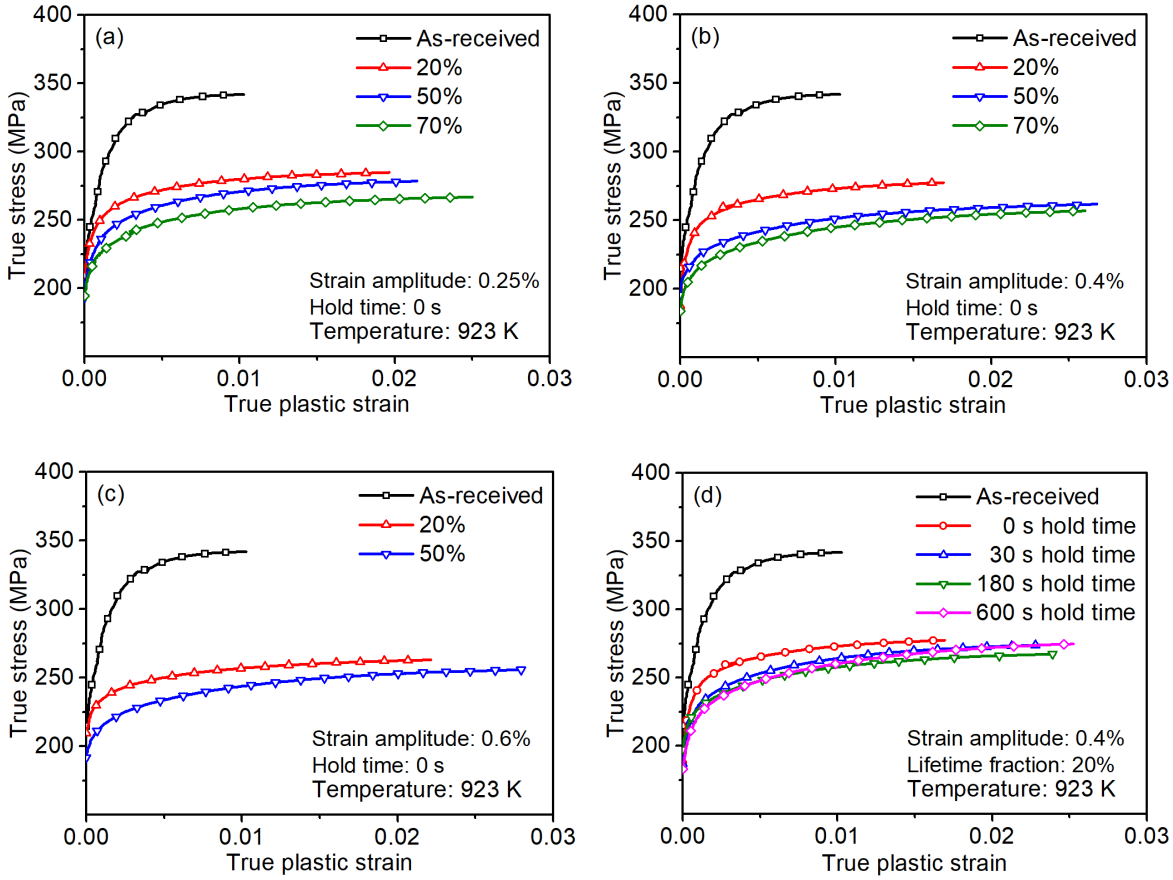

Fig. 4. True tensile curves after various prior fatigue loading conditions: (a) 0.25% strain amplitude prior LCF loading, (b) 0.4% strain amplitude prior LCF loading, (c) 0.6% strain amplitude prior LCF loading, (d) 20% lifetime fraction prior C-F loading

3. Constitutive models

3.1 Johnson–Cook constitutive model

The JC model is capable of describing isotropic hardening, strain rate hardening and thermal softening, and it has been widely used because of its simplicity and the availability of model parameters (Samantaray et al., 2009). As a result, its extended or modified models have also been successfully developed for various materials (Zhang et al., 2009; Vural et al., 2009). Therefore, the JC model was selected as the fundamental model in the current study. The original JC model can be expressed as:

$$\sigma(\varepsilon^{\mathrm{p}},\dot{\varepsilon},T)=\left(A+B\left(\varepsilon^{\mathrm{p}}\right)^{n}\right)\left(1+C\ln\left(\frac{\dot{\varepsilon}}{\dot{\varepsilon}_0}\right)\right)\left(1-\left(\frac{T-T_R}{T_m-T_R}\right)^{m}\right) \tag{3}$$

where σ is the flow stress, A is the yield stress at reference temperature and reference strain rate, B is the strain-hardening coefficient, ε^{p} is the plastic strain, n is the strain hardening exponent, C is material constant which represents the coefficient of strain rate hardening, $\dot{\varepsilon}$ is the strain rate, $\dot{\varepsilon}_0$ is the reference strain rate, T is the current kelvin temperature, T_{R} is the reference temperature, T_{m} is the melting temperature, and m is the material constant, which represents the thermal softening exponent (Samantaray et al., 2009). The items $A+B\left(\varepsilon^{\mathrm{p}}\right)^{n}$, $1+C\ln\left(\frac{\dot{\varepsilon}}{\dot{\varepsilon}_0}\right)$ and $1-\left(\frac{T-T_R}{T_m-T_R}\right)^{m}$ describe the effect of strain hardening, strain rate and temperature, respectively.

3.2 Moćko's model

As observed, the remnant tensile deformation behaviour was altered by prior fatigue loading. Consequently, Moćko et al. (Moćko et al., 2016; Moćko et al., 2017) modified the original JC model to take into account the effects of prior fatigue loading, see Eqs. (4)-(7). Moćko's model consists of three modified equations. The large number of modified equations and many fitting parameters undoubtedly provide good simulation results (Moćko et al., 2016; Moćko et al., 2017), however, they make the model complicated and inconvenient for practical application. To evaluate the capacity of Moćko's model at high temperature and strain-controlled fatigue loading conditions, the predicted results by Moćko's model were also presented for comparison in the current study, which will be discussed in the Section 4.2.

$$\sigma(\varepsilon^{\mathrm{p}},\dot{\varepsilon},T)=\left(A+B\left(\varepsilon^{\mathrm{p}}\right)^{n}\right)\left(1+C\ln\left(\frac{\dot{\varepsilon}}{\dot{\varepsilon}_0}\right)\right)\left(1-\left(\frac{T-T_R}{T_m-T_R}\right)^{m}\right) \tag{4}$$

$$A(\alpha_A,\beta_A,D,\chi_A,\sigma_0,\sigma,\delta_A)=A_0+\alpha_A\left(1-\exp\left(-\beta_A D\right)\right)+\chi_A\left(\frac{\sigma}{\sigma_0}-1\right)+\delta_A D \tag{5}$$

$$B(\alpha_B,\beta_B,D,\chi_B,\sigma_0,\sigma,\delta_B)=B_0+\alpha_B\left(1-\exp\left(-\beta_B D\right)\right)+\chi_B\left(\frac{\sigma}{\sigma_0}-1\right)+\delta_B D \tag{6}$$

$$n(\alpha_n,\beta_n,D,\chi_n,\sigma_0,\sigma,\delta_n)=n_0+\alpha_n\left(1-\exp\left(-\beta_n D\right)\right)+\chi_n\left(\frac{\sigma}{\sigma_0}-1\right)+\delta_n D \tag{7}$$

where α, β, and χ are coefficients of the equation which represent cyclic hardening of the material at the initial stage of cyclic deformation, δ represents the development rate of fatigue damage, D is the coefficient of accumulative fatigue damage, σ_0 is reference value of the maximum cyclic stress, and σ is the maximum cyclic stress (Moćko et al., 2016).

3.3 Fatigue damage parameter

During fatigue process of 9%Cr steel, the cyclic softening occurs, which has been validated by many studies (Fournier et al., 2011; Shankar et al., 2006). The microstructure evolution (recovery of martensite lath structure and decrease of dislocation density) contributes to the softening behaviour and results in alternation of inelastic strain range in the fatigue process (Wang et al., 2019). The typical strain-controlled strain-stress hysteresis loop and inelastic strain range of 9%Cr steel during LCF and C-F processes are shown in Figs. 5(a) and (b), respectively. It is noteworthy that the inelastic strain range is varied with respect to the fatigue cycle. Fig. 6 further depicts the evolution of the inelastic strain range at various fatigue loading conditions. The higher the lifetime fraction, the larger the inelastic strain range was observed. Moreover, the increase in strain amplitude led to an evident increase in the inelastic strain range. Nevertheless, the inelastic strain range at various hold times did not differ widely, which suggests that the additional inelastic deformation introduced by the hold period of C-F loading is quite small. This phenomenon is in agreement with microstructural observations (Zhang et al., 2019) and the tensile curves observed in Figs. 3 and 4. Consequentially, it may be reasonable to utilize the inelastic strain range to evaluate the fatigue damage.

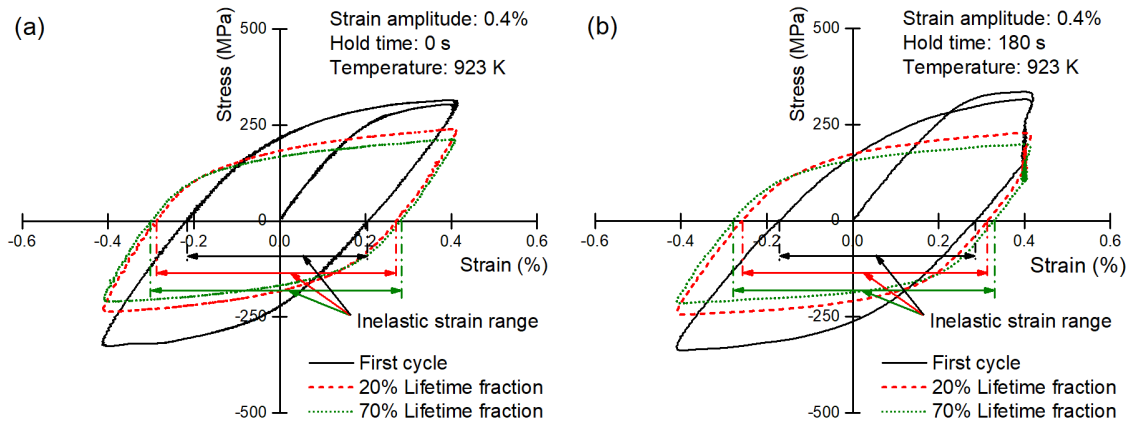

Fig. 5. Typical strain-controlled strain-stress hysteresis loops of the as-received P92 steel at (a) LCF and (b) C-F loading conditions

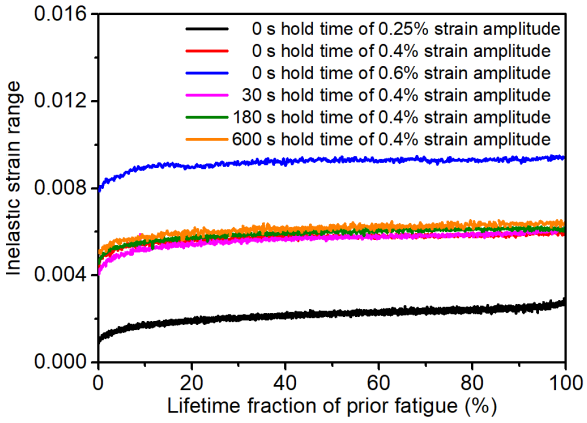

Fig. 6. Evolution of the inelastic strain range at various prior fatigue loading conditions

Based on the inelastic strain range in the first cycle and failure cycle, a fatigue damage parameter was defined in our previous works (Wang et al., 2019; Zhang et al., 2019) and is given as:

$$D_{\mathrm{F}} = \frac{\varepsilon_{in}^{n} - \varepsilon_{in}^{0}}{\varepsilon_{in}^{f} - \varepsilon_{in}^{0}} \tag{8}$$

where D_{F} is the defined fatigue damage parameter ($0 \le D_{\mathrm{F}} \le 1$) and ε_{in}^{0}, ε_{in}^{f} and ε_{in}^{n} are the inelastic strain range in the first cycle, the failure cycle and the studied cycle, respectively. Fig. 7 depicts the evolution of the defined fatigue damage at various prior fatigue loading conditions. It is shown that the defined fatigue damage increases rapidly in the initial stage and tends to be stable as the lifetime fraction increases further, which has been demonstrated to correspond to the decline of dislocation density (Wang et al., 2019).

Moreover, the increase in strain amplitude leads to the increase of defined fatigue damage. Nevertheless, defined fatigue damage does not vary significantly with increased hold time, which is in agreement with the evolution of the inelastic strain range shown in Fig. 6. It demonstrates that, within 600 s, the damage introduced by the hold period is limited and the damage mechanism of the prior C-F loading is still dominated by the fatigue process rather than the hold process (creep), which has been proved by microstructural analysis (Zhang et al., 2019).

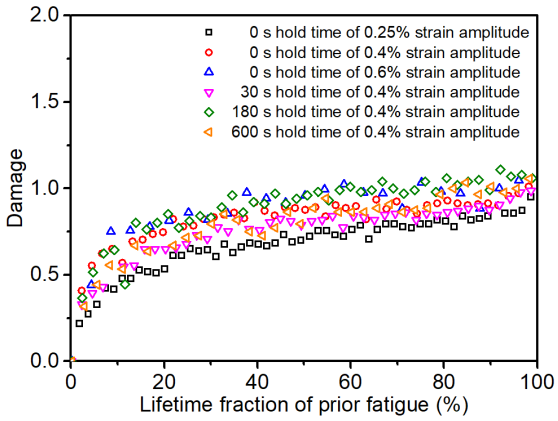

Fig. 7 Evolution of the defined fatigue damage at various prior fatigue loading conditions

The relationships between tensile strength, microstructure features and the defined fatigue damage were further compared here to validate the reliability of the defined fatigue damage parameter. Figs. 8(a) and (b) show the relationship between the defined fatigue damage and the 0.2% offset yield stress and the ultimate tensile stress, respectively. Note that both the yield stress and ultimate tensile stress show linear behaviour with respect to the defined fatigue damage, regardless of the variation in hold time and the strain amplitude. This suggests that the defined fatigue damage parameter can describe remnant tensile strength well. Since the degradation of remnant tensile strength is mainly attributed to microstructure evolution, namely, the decline in dislocation density and recovery of the martensite lath width, the capacity of the defined fatigue damage parameter to capture the microstructure evolution (Table 1) should also be verified. Fig. 9 presents the variation in the martensite lath width and the dislocation density with respect to the defined fatigue damage.

The martensite lath width and the dislocation density were summarized from our previous works (Wang et al., 2019; Zhang et al., 2019) and references (Barrett et al., 2017). The dislocation density varies linearly with the defined fatigue damage, as shown in Fig. 9(b). However, the relationship between the martensite lath width and the defined fatigue damage shows an exponential trend, as shown in Fig. 9(a). According to Hall-Petch effect (Morito et al., 2019; Shi et al., 2019), material strength is proportional to the $d^{-1/2}$, where d is the width of martensite lath. Therefore, the relationship between $d^{-1/2}$ and the defined fatigue damage parameter is presented, as shown in Fig. 9(a), inserted figure. The linear behaviour between $d^{-1/2}$ and the defined fatigue damage parameter can be observed, irrespective of the strain amplitude and hold time. Consequently, it can be concluded that the defined fatigue damage parameter is robust in describing the damage evolution of the LCF and C-F loadings and it is therefore reasonable to use the defined fatigue damage parameter to modify the JC model for simulating remnant tensile deformation.

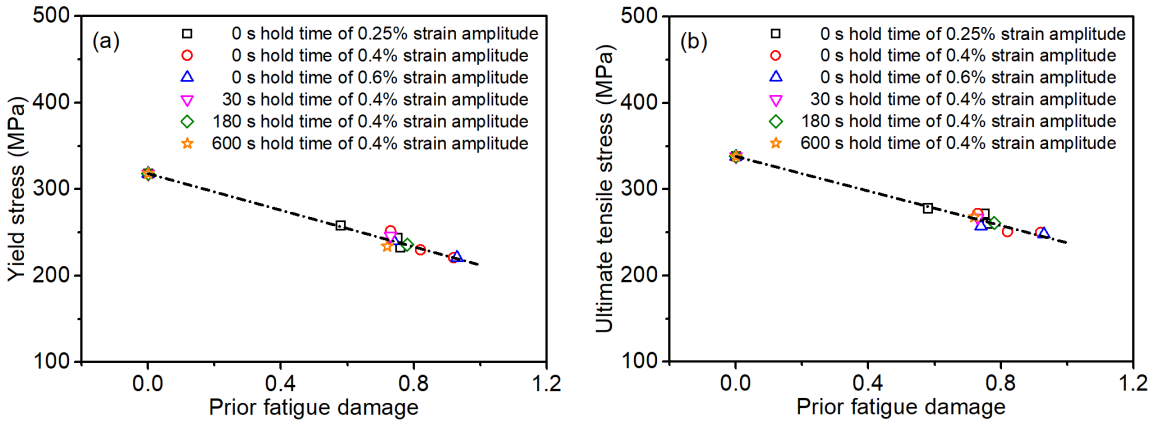

Fig. 8. Relationship between the defined prior fatigue damage and (a) yield stress and (b) ultimate tensile stress.

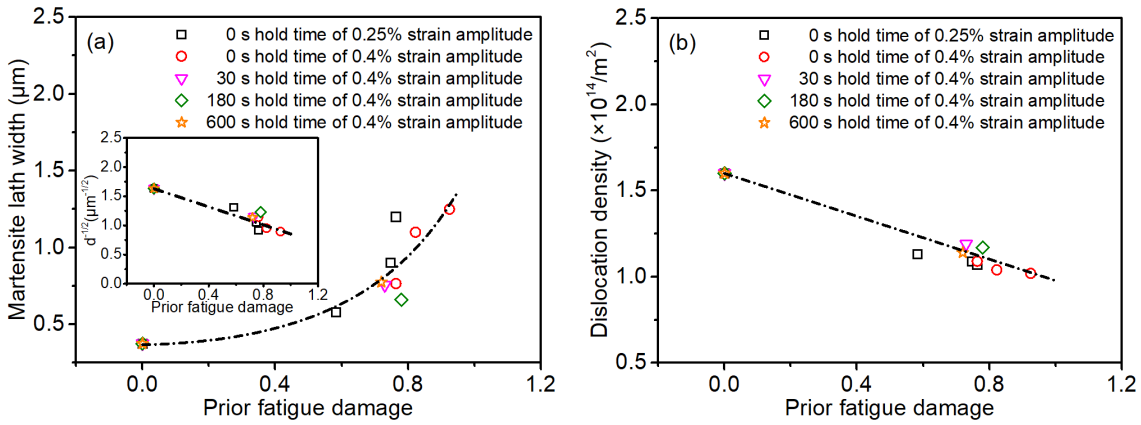

Fig. 9. Relationship between (a) martensite lath width, (b) dislocation density and the defined prior fatigue damage.

3.4 Modification of JC model for different loading conditions

As mentioned above, the strain hardening behaviour of 9%Cr steel is weakened by the prior fatigue loading due to the decline of dislocation density. This effect dramatically influences subsequent tensile deformation. Therefore, the item $A+B\left(\varepsilon^{\mathrm{p}}\right)^{n}$, which describe the effect of strain hardening, should be modified to account for prior fatigue loading effects. In the present work, a modified JC model is proposed to describe the tensile deformation after prior fatigue loading and is expressed as:

$$\sigma(\varepsilon^{\mathrm{p}},\dot{\varepsilon},T)=\left(A+B_1\left(\varepsilon^{\mathrm{p}}\right)^{n_1}+B_2\exp\left(n_2\varepsilon^{\mathrm{p}}\right)\right)\left(1+C\ln\left(\frac{\dot{\varepsilon}}{\dot{\varepsilon}_0}\right)\right)\left(1-\left(\frac{T-T_R}{T_m-T_R}\right)^{m}\right) \tag{9}$$

where the item $B_2\exp\left(n_2\varepsilon^{\mathrm{p}}\right)$ is introduced to account for the effects of prior fatigue loading on strain hardening, B_2 and n_2 are material constants, and B_1 and n_1 are material constants that are identical with the B and n in Eq. (3). Since the reference and test strain rates taken as the same value in the present work ($\dot{\varepsilon}=\dot{\varepsilon}_0$ =0.001), the modified model can be therefore reduced to:

$$\sigma(\varepsilon^{\mathrm{p}},T)=\left(A+B_1\left(\varepsilon^{\mathrm{p}}\right)^{n_1}+B_2\exp\left(n_2\varepsilon^{\mathrm{p}}\right)\right)\left(1-\left(\frac{T-T_R}{T_m-T_R}\right)^{m}\right) \tag{10}$$

The material parameters in the modified JC model are decided with the following steps:

(1) The parameters: A, T_R and T_m

In the present study, the reference temperature T_R is taken as 293 K, the yield stress A at reference temperature and reference strain rate is then determined from tensile curves at 293 K (A=641 MPa), as shown in Fig. 10, which is the 0.2% offset yield stress. For 9%Cr steel, the melting temperature T_m is taken as 1773 K (Francis et al., 2006).

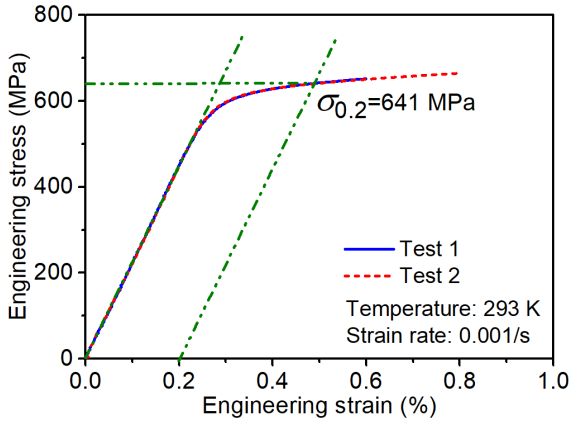

Fig. 10. Determination of yield stress of P92 steel at 293 K

(2) The parameter: m

When prior fatigue damage is set as 'zero', the item $B_2 \exp\left(n_2 \varepsilon^p\right)$ is eliminated and ε^p=0, Eq. (10) becomes:

$$\sigma(\varepsilon^p, T)=A\left(1-\left(\frac{T-T_R}{T_m-T_R}\right)^m\right) \tag{11}$$

By fitting the true tensile curves of the as-received specimen at 923 K, as presented in Fig. 4 (black line), the temperature sensitivity parameter m can be obtained.

(3) The remaining parameters: B_1, n_1, B_2 and n_2

As the parameters, A, T_R, T_m and m have been determined, the remaining parameters, B_1, n_1, B_2, and n_2, can be obtained by fitting the true tensile curves after prior fatigue loading. The experimental tensile results after 0.4% strain amplitude prior LCF loading (Fig. 4(b)) were used here. During all fitting procedures, the

optimization program was implemented in MATLAB software with a gradient-based Levenberg-Marquardt algorithm, which aimed to seek the minimum differences between experimental and simulated results. At each loading condition, one set of parameters B_1, n_1, B_2 and n_2 will be obtained. The obtained parameters of the proposed model are listed in Table 2.

Table 2 Parameters of the proposed model for 9%Cr steel at 923 K

Test No.	Defined damage	A (MPa)	B_1 (MPa)	n_1	B_2 (MPa)	n_2	m	T_R (K)	Tm (K)
1	As-received	641	1817	0.3	-277	41	0.8	293	1773
2	0.73	641	831	0.25	-298	14.6	0.8	293	1773
3	0.82	641	697	0.35	-253	7.6	0.8	293	1773
4	0.92	641	707	0.32	-285	6.7	0.8	293	1773

As mentioned above, the defined fatigue damage parameter can account for the effects of various prior fatigue loadings and its robustness has been validated. Therefore, the defined fatigue damage parameter will be adopted by the proposed model to account for the effects of various prior fatigue loadings. Fig. 11 depicts the relationships between the defined fatigue damage and the determined model parameters. It is interesting to find that the parameters n_1 and B_2 almost stay constant with respect to the defined fatigue damage values, which are 0.3 MPa and -277 MPa, respectively, as shown in Figs. 11(b) and (c). Moreover, the parameters B_1 and n_2 present a linear behaviour with increasing prior fatigue damage. By fixing the parameters n_1 and B_2 at 0.3 MPa and -277 MPa, respectively, the value of parameters B_1 and n_2 can be then determined by the aforementioned optimization program. The determined model parameters are shown in Fig. 12 and listed in Table 3. Linear relationships between the defined fatigue damage and parameters B_1 and n_2 can also be observed. Finally, two linear equations obtained by least-squares linear regression were used to describe the evolutions, as shown in Fig. 12 and given as

$$B_1=\alpha_{B1}+\beta_{B1}\times D_F \tag{12}$$

$$n_2=\alpha_{n2}+\beta_{n2}\times D_F \tag{13}$$

where α_{B1}=1809 MPa, β_{B1}=-1358 MPa, α_{n2}=42, β_{n2}=-42. Consequently, the final parameters of the proposed model for 9%Cr steel at 923 K can be determined, as listed in Table 4.

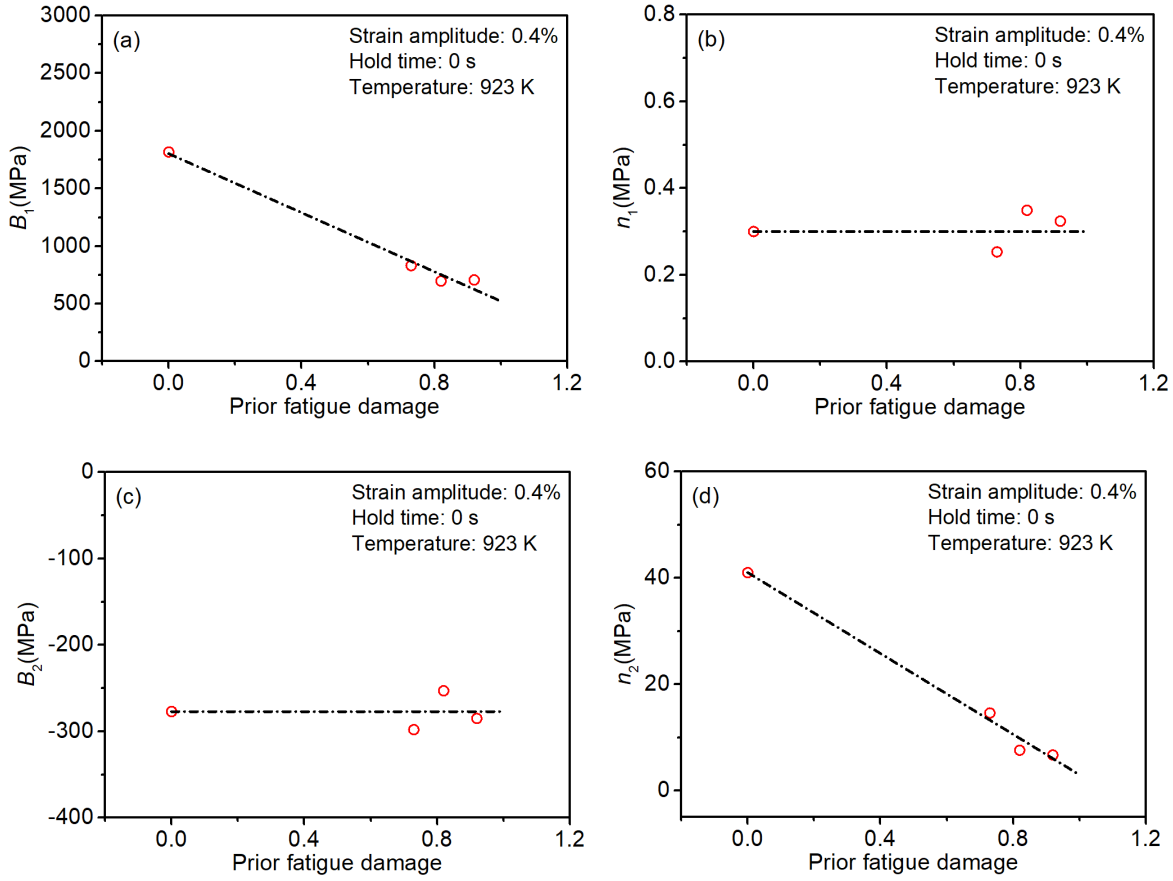

Fig. 11. Relationship between prior fatigue damage and the material constants of the proposed model (a) B_1, (b) n_1, (c) B_2 and (d) n_2

Table 3 Modified parameters of the proposed model for 9%Cr steel at 923 K

Test No.	Defined damage	A (MPa)	B_1 (MPa)	n_1	B_2 (MPa)	n_2	m	T_R (K)	Tm (K)
1	As-received	641	1817	0.3	-277	41	0.8	293	1773
2	0.73	641	974	0.3	-277	18	0.8	293	1773
3	0.82	641	662	0.3	-277	7.5	0.8	293	1773
4	0.92	641	557	0.3	-277	3.9	0.8	293	1773

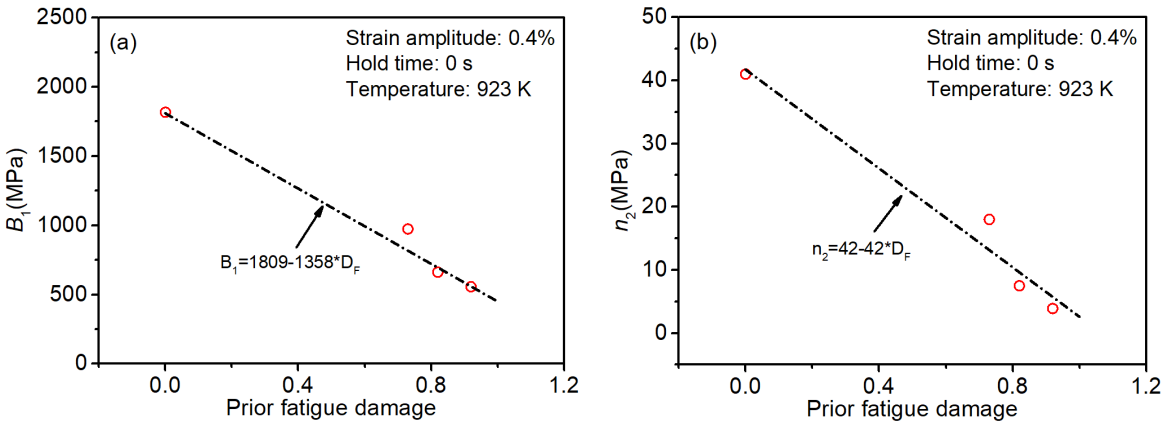

Fig. 12. Modified relationship between prior fatigue damage and the material constants of the proposed model (a) B_1, (b) n_2

Table 4 Final parameters of the proposed model for 9%Cr steel at 923 K

Material constants	A (MPa)	α_{B1} (MPa)	β_{B1} (MPa)	n_1	B_2 (MPa)	α_{n2}	β_{n2}	m	T_R (K)	Tm (K)
Values	641	1809	-1358	0.3	-277	42	-42	0.8	293	1774

4. Simulation results and discussion

4.1. Parameter sensitivity analysis

The objective of the sensitivity analysis is to validate the reliability of the proposed model and determine the effect of the studied parameters on modelling. In the present study, since parameters B_2 and n_1 are constants, the sensitivity analysis focuses on parameters B_1 and n_2. The influence of various parameters on the tensile curves is shown in Fig. 13. The tensile curve of 70% lifetime fraction of 0.4% strain amplitude prior LCF loading was selected as example. Parameters B_1 and n_2 are independent variables in these plots. These results provide primary judgement regarding the effects of these parameters on tensile deformation. From Fig. 13, the proposed model is shown to be more sensitive to parameter B_1 than n_2. Therefore, parameter B_1 should be determined carefully according to the procedure described in Section 3.4.

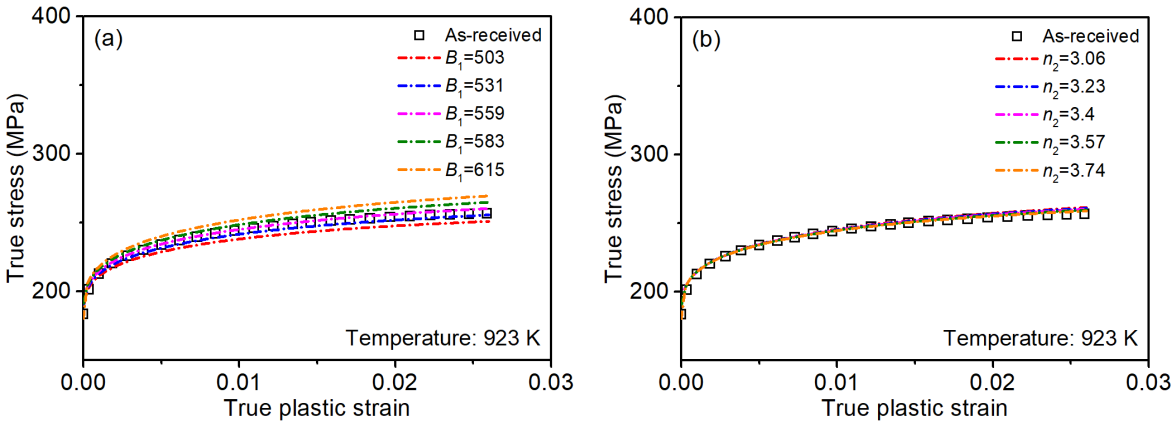

Fig. 13. Comparison of tensile curves at various parameters (a) B_1, (b) n_2

4.2. Validation of model accuracy

In this section, model validation is conducted by comparing experimental tensile curves and simulated results. Experimental tensile curves under 0.4% strain amplitude prior LCF loading, which were utilized to determine model parameters, were used to perform the validation. Simulated results were calculated by the three models (original JC model, Moćko's model and the proposed model) described in Section 3. The original JC and Moćko's model parameters were determined through the referenced methods (Johnson et al., 1985; Moćko et al., 2016; Moćko et al., 2017) using the aforementioned optimization program. The material parameters used in the three constitutive models for 9%Cr steel at 923 K are finally identified and listed in Table 5. Since the experiments in the present study were performed under strain control, the items relating to stress-controlled factors in Moćko's model were not considered here (χ_A=χ_B=χ_n=0, σ_0=1). Fig. 14 presents the comparison of tensile curves between experimental results and simulated data. Fig. 14(c) indicates that the proposed model is adequate to describe the tensile deformation after various lifetime fraction prior fatigue loadings. Compared to the proposed model, the original JC model fails to reproduce the tensile deformation under prior fatigue loading due to the absence of consideration on prior fatigue loading, as shown in Fig. 14(a). The predicted tensile curves at various lifetime fractions by the original JC model overlap with each

other. It is also worth noting that Moćko's model is relatively imprecise in comparison with the proposed model, as presented in Fig. 14(b). Although Moćko's model can account for the effects of prior fatigue loading, evident deviation between simulated and experimental data can be observed. Yet, Moćko's model performs better than the original JC model. Importantly, Moćko's model was determined at room temperature, however, the experiments of the presents work were conducted at high temperature, thus the deviation of the simulated results from Moćko's model may be ascribed to the thermal effect. At high temperature, the resistance of the material to deformation decreases because dislocation movement occurs more readily, and hence inelastic deformation is enhanced (Lee et al., 2006; Gambirasio et al., 2016). This problem may have a significant impact on the expression of the constitutive model determined at low temperature. Therefore, Moćko's model does not function well at high temperature. In addition, a large number of material parameters in Moćko's model (a total number of 17 material parameters, Table 5) make it hard to use. Regarding the proposed model, few material parameters (a total number of 8 material parameters, Table 5) are required and a good simulation results can be obtained, which suggests that the proposed model is relatively convenient and reliable to use.

Table 5 Parameters of different constitutive models for 9%Cr steel at 923 K

Model	Parameters				Shared parameters
JC model	A=641 MPa	B=2017 MPa	n=0.22	m=0.35	
Moćko's model	A_0=641 MPa	B_0=2017 MPa	n_0=0.22	σ_0=1	T_R=293 T_m=1774
	α_A=-97 MPa	β_A=73 MPa	χ_A=0	δ_A=127 MPa	
	α_B=-0.02 MPa	β_B=-10 MPa	χ_B=0	δ_B=-1671 MPa	
	α_n=-0.25	β_n=79905	χ_n=0	δ_n=0.26	
	m=0.35				
Proposed model	A=641 MPa	α_{B1}=1809	β_{B1}=-1358 MPa	n_1=0.3	
	B_2=-277 MPa	α_{n2}=42	β_{n2}=-42	m=0.8	

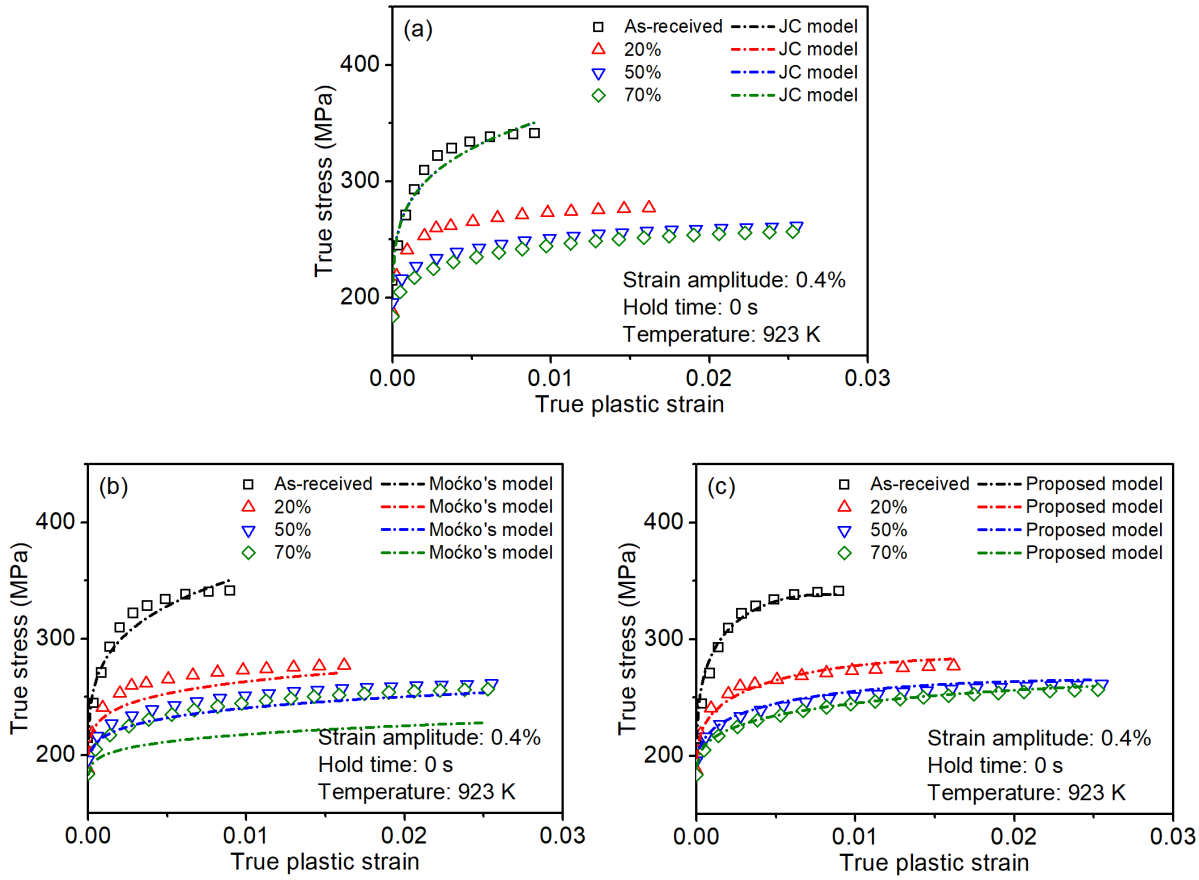

Fig. 14. Comparisons between simulated tensile curves produced by different models at 0.4% strain amplitude prior LCF loading (a) JC model, (b) Moćko's model and (c) Proposed model

To further verify the reliability of the proposed model, the average error ($\bar{\Delta}$) and standard deviation (S) between experimental and predicted data of the three models were compared. The average error ($\bar{\Delta}$) and standard deviation (S) are expressed respectively as:

$$\bar{\Delta}=\frac{1}{N}\sum_{i=1}^{i=N}\left|\frac{\sigma_{Exp}-\sigma_{P}}{\sigma_{Exp}}\right| \tag{14}$$

$$S=\sqrt{\frac{\sum_{i=1}^{i=N}\left(\Delta_{i}-\bar{\Delta}\right)^{2}}{N-1}} \tag{15}$$

where σ_{Exp} and σ_{P} are experimental stress and predicted stress, respectively, N is the number of samples. The obtained average error ($\bar{\Delta}$) and standard deviation (S) between experimental and predicted results of the three models are listed in Table 6. It can be observed that not only the average error ($\bar{\Delta}$) but also the standard

deviation (S) of the proposed model is the lowest compared to the original JC model and Moćko's model, which validates the reliability of the proposed model as well. Nevertheless, the experimental results simulated here were utilized for the determination of material parameters, predictive capacity of the proposed model should be verified further by experimental data which was not used to determine the material parameters.

Table 6 Average error ($\bar{\Delta}$) and standard deviation (S) between predicted and experimental data at various fatigue lifetime fractions of 0.4% strain amplitude prior LCF loading

Model	Average error ($\bar{\Delta}$)				Standard deviation (S)			
Lifetime fraction	As-received	20%	50%	70%	As-received	20%	50%	70%
JC model	0.0270	0.2504	0.4101	0.4452	0.0197	0.0722	0.0965	0.0846
Moćko's model	0.0270	0.0374	0.0373	0.1004	0.0197	0.0129	0.0082	0.0234
Proposed model	0.0195	0.0157	0.0145	0.0062	0.0135	0.0080	0.0064	0.0064

4.3. Capability of the proposed model

The objective here is to assess the predictive capability of the proposed model. As discussed above, the simulated ability of the proposed model under 0.4% strain amplitude prior LCF loading, which was utilized to determine model parameters, has been verified. The challenge now is to evaluate the proposed model's capacity to predict the tensile deformation at different strain amplitudes and different hold times of prior fatigue loading. In this section, the same set of parameters listed in Table 4 was used.

Fig. 15(a), (b) and (c) present the predicted results of tensile curves at 0.25% strain amplitude prior LCF loading, 0.6% strain amplitude prior LCF loading, and 20% lifetime fraction prior C-F loading, respectively. An overall observation indicates that the proposed model gives a satisfactory prediction for tensile deformation at other prior fatigue loading conditions. Not only the effect of low strain amplitude prior LCF loading (Fig. 15(a)) but also the effect of high strain amplitude prior LCF loading (Fig. 15(b)) can be well captured by the proposed model. Additionally, the tensile deformation after various prior C-F loadings,

which hold time ranges from 0 s to 600 s, can be reproduced by the proposed model as well, as shown Fig. 15(c). This is attributed to the defined fatigue damage parameter is independent on fatigue loading conditions. Furthermore, the average error ($\bar{\Delta}$) and standard deviation (S) results presented in Table 7 also validate that the proposed model can give satisfactory prediction for tensile deformation at various prior fatigue loadings. Hence, it can be concluded that the proposed model is robust to precisely predict the tensile deformation of 9%Cr steel under prior fatigue loading.

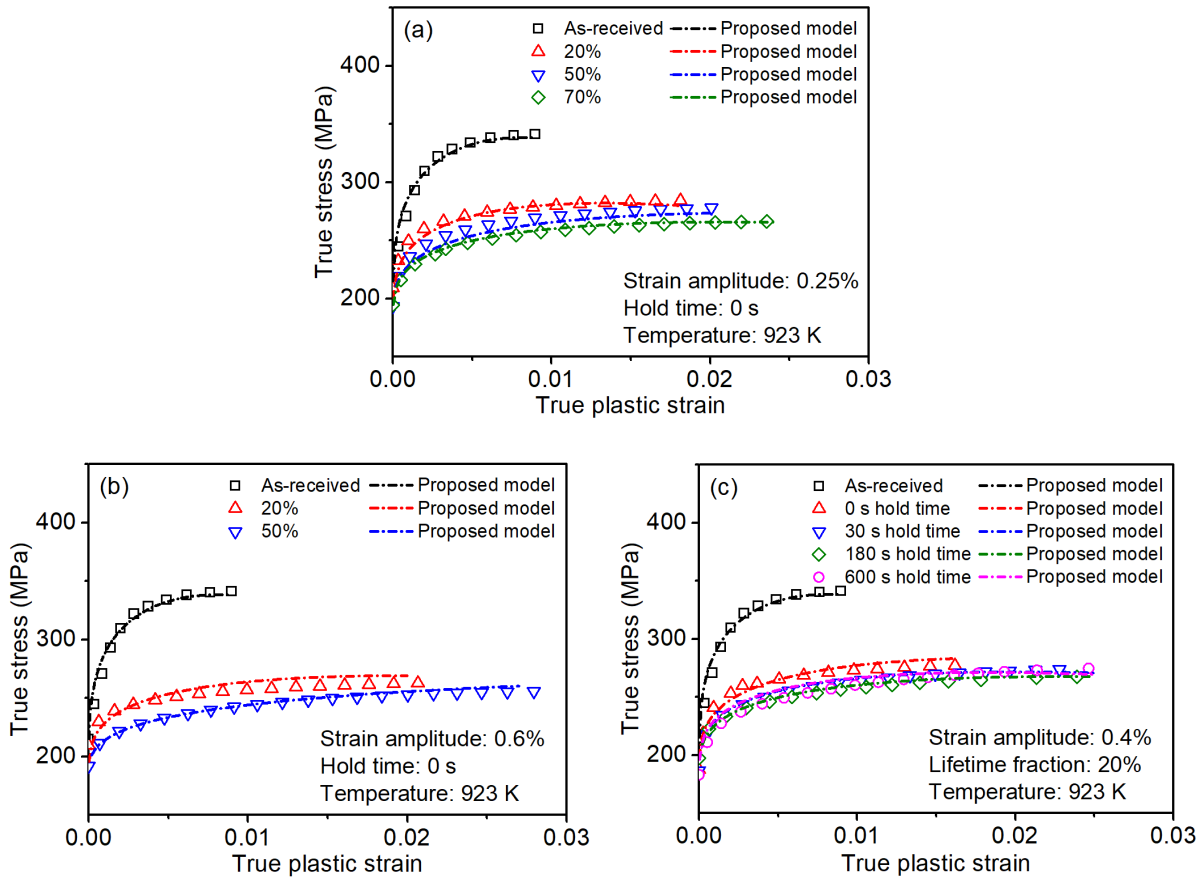

Fig. 15. Comparison of experimental tensile curves and predicted tensile curves at various prior fatigue loading conditions: (a) 0.25% strain amplitude prior LCF loading, (b) 0.6% strain amplitude prior LCF loading, (c) 20% lifetime fraction prior C-F loading

Table 7 Average error ($\bar{\Delta}$) and standard deviation (S) between predicted and experimental data of the proposed model at various loading conditions

Loading conditions	Average error ($\bar{\Delta}$)				Standard deviation (S)			
	As-received	20%	50%	70%	As-received	20%	50%	70%
0.25% strain amplitude prior LCF loading	0.0195	0.0122	0.0202	0.0056	0.0135	0.0140	0.0066	0.0046
0.4% strain amplitude prior LCF loading	0.0195	0.0157	0.0145	0.0062	0.0135	0.0080	0.0064	0.0064
0.6% strain amplitude prior LCF loading	0.0195	0.0239	0.0069	/	0.0135	0.0118	0.0069	/
	As-received	30 s	180 s	600 s	As-received	30 s	180 s	600 s
20% lifetime fraction prior C-F loading	0.0195	0.0073	0.0067	0.0243	0.0135	0.0084	0.0055	0.0171

5. Conclusions and remarks

In the present study, a modified constitutive model for the tensile deformation of 9%Cr steel under prior fatigue loading was proposed based on the Johnson-Cook model. In the proposed model, a strain hardening rule combined with a defined fatigue damage parameter were introduced to account for the effects of prior fatigue loading. The defined fatigue damage parameter comprehensively enhances the predictive capacity of the proposed model at various prior fatigue loading conditions.

Fewer material parameters are involved in the proposed model in comparison with Moćko's model. The proposed model is capable of predicting the tensile deformation under different lifetime fractions, strain amplitudes and hold times of prior fatigue loading. However, the proposed model needs further validation under other prior fatigue loading conditions, such as under different temperatures and different strain rates. These points will be investigated in the future.

Acknowledgements

The authors gratefully acknowledge the financial support of the National Key R&D Program of China (No. 2018YFC0808800), China Postdoctoral Science Foundation (No. 2016M600405) and innovation

program for graduate students in Jiangsu Province of China (No. KYCX17_0935). We also thank the support from China Scholarship Council (CSC) and the University of Strathclyde.

References

Livatyali, H., Altan, T., 2001. Prediction and elimination of springback in straight flanging using computer aided design methods: Part 1. Experimental investigations. J. Mater. Process. Tech. 17(1-2), 262-268. https://doi.org/10.1016/S0924-0136(01)01164-5

Sánchez-Santana, U., Rubio-González, C., Mesmacque, G., Amrouche, A.,2009. Effect of fatigue damage on the dynamic tensile behavior of 6061-T6 aluminum alloy and AISI 4140T steel. Int. J. Fatigue 31(11-12), 1928-1937. https://doi.org/10.1016/j.ijfatigue.2009.02.031

Sánchez-Santana, U., Rubio-González, C., Mesmacque, G., Amrouche, A., Decoopman, X., 2008. Effect of fatigue damage induced by cyclic plasticity on the dynamic tensile behavior of materials. Int. J. Fatigue 30(10-11), 1708-1719. https://doi.org/10.1016/j.ijfatigue.2008.03.011

Sánchez-Santana, U., Rubio-González, C., Mesmacque, G., Amrouche, A., Decoopman, X., 2008. Dynamic tensile behavior of materials with previous fatigue damage. Mater. Sci. Eng., A 497(1-2), 51-60. https://doi.org/10.1016/j.msea.2008.07.063

Moćko, W., 2014. The influence of stress-controlled tensile fatigue loading on the stress–strain characteristics of AISI 1045 steel. Mater. Des. 58, 145-153. https://doi.org/10.1016/j.matdes.2014.02.021

Moćko, W., Kowalewski, Z. L., 2014. Evolution of tensile properties of the TiAl6V4 alloy due to the prior cyclic loading history. J. Theor. App. Mech. 52, 847-851. bwmeta1.element.baztech-4bdd7117-d15b-4063-ad94-d7bf87c3fe38

Moćko, W., Brodecki, A., Radziejewska, J., 2015. Effects of pre-fatigue on the strain localization during tensile tests of DP 500 steel at low and high strain rates. J. Strain. Anal. Eng. Des.50(8), 571-583. https://doi.org/10.1177/0309324715599132

Moćko, W., Brodecki, A., Kruszka, L., 2016. Mechanical response of dual phase steel at quasi-static and dynamic tensile loadings after initial fatigue loading. Mech. Mater. 92, 18-27. https://doi.org/10.1016/j.mechmat.2015.07.015

Mariappan, K., Shankar, V., Sandhya, R., Mathew, M. D., Bhaduri, A. K., 2015. Influence of prior fatigue damage on tensile properties of 316L (N) stainless steel and modified 9Cr-1Mo steel. Metall. Mater. Trans. A 46(2), 989-1003. https://doi.org/10.1007/s11661-014-2676-4

Mariappan, K., Shankar, V., Sandhya, R., Bhaduri, A. K., Laha, K., 2016. A Comparative Evaluation of the Effect of Low Cycle Fatigue and Creep–Fatigue Interaction on Surface Morphology and Tensile Properties of 316L (N) Stainless Steel. Metall. Mater. Trans. A 47(4), 1575-1586. https://doi.org/10.1007/s11661-015-3270-0

Mariappan, K., Shankar, V., Sandhya, R., Bhaduri, A. K., Laha, K., 2017. Comparative assessment of remnant tensile properties of modified 9Cr-1Mo steel under prior low cycle fatigue and creep-fatigue interaction loading. Int. J. Fatigue 03, 342-352. https://doi.org/10.1016/j.ijfatigue.2017.05.013

Paul, S. K., Sivaprasad, S., Dhar, S., Tarafder, S., 2010. Cyclic plastic deformation and cyclic hardening/softening behavior in 304LN stainless steel. Theor. Appl. Fract. Mec. 54(1), 63-70. https://doi.org/10.1016/j.tafmec.2010.06.016

Paul, S. K., Sivaprasad, S., Dhar, S., Tarafder, S., 2011. Cyclic plastic deformation and damage in 304LN stainless steel. Mater. Sci. Eng., A 528(15), 4873-4882. https://doi.org/10.1016/j.msea.2011.03.048

Hamdoon, M., Das, S., Zamani, N., Grenier, D., 2011. Experimental study on the effect of strain cycles on mechanical properties of AISI 1022 steel. Strain 47, 386-392. https://doi.org/10.1111/j.1475-1305.2010.00781.x

Zhang, W., Wang, X., Chen, H., Zhang, T., Gong, J., 2019. Evaluation of the effect of various prior creep-fatigue interaction damages on subsequent tensile and creep properties of 9%Cr steel. Int. J. Fatigue 125, 440-453. https://doi.org/10.1016/j.ijfatigue.2019.04.018.

Johnson, G. R., Cook, W. H., 1985. Fracture characteristics of three metals subjected to various strains, strain rates, temperatures and pressures. Eng. Fract. Mech. 21(1), 31-48. https://doi.org/10.1016/0013-7944(85)90052-9

Zerilli, F. J., Armstrong, R. W., 1987. Dislocation-mechanics-based constitutive relations for material dynamics calculations. J. Appl. Phys. 61(5), 1816-1825. https://doi.org/10.1063/1.338024

Khan, A. S., Huang, S., 1992. Experimental and theoretical study of mechanical behavior of 1100 aluminum in the strain rate range 10^{-5}– 10^{4} s^{-1}. Int. J. Plast. 8(4), 397-424. https://doi.org/10.1016/0749-6419(92)90057-J

Meyers, M. A., 1994. Dynamic behavior of materials. John wiley & sons.

Nemat-Nasser, S., Li, Y., 1998. Flow stress of fcc polycrystals with application to OFHC Cu. Acta. Mater. 46(2), 565-577. https://doi.org/10.1016/S1359-6454(97)00230-9

Preston, D. L., Tonks, D. L., Wallace, D. C., 2003. Model of plastic deformation for extreme loading conditions. J. Appl. Phys. 93(1), 211-220. https://doi.org/10.1063/1.1524706

Lin, Y. C., Chen, X. M., 2011. A critical review of experimental results and constitutive descriptions for metals and alloys in hot working. Mater. Des. 32(4), 1733-1759. https://doi.org/10.1016/j.matdes.2010.11.048

Mońko, W., Grzywna, P., Kowalewski, Z. L., Radziejewska, J., 2016. An influence of cyclic loading on the form of constitutive relationship for DP500 steel. Mater. Des. 103, 183-193. https://doi.org/10.1016/j.matdes.2016.04.075

Mońko, W., Kruszka, L., 2017. A viscoplastic response of a dual phase steel exposed to prior cyclic loadings. Mech. Mater. 113, 126-135. https://doi.org/10.1016/j.mechmat.2017.07.019

Wang, X., Zhang, W., Ni, J., Zhang, T., Gong, J., Wahab, M. A., 2019. Quantitative description between pre-fatigue damage and residual tensile properties of P92 steel. Mater. Sci. Eng., A 744, 415-425. https://doi.org/10.1016/j.msea.2018.12.029

ASTM standard E2714, 2014. Standard test method for creep-fatigue testing. ASTM international, West Conshohocken, PA. https://doi.org/10.1520/E2714-09

ASTM Standard E8, 2004. Standard test methods for tension testing of metallic materials. ASTM international, West Conshohocken, PA. https://doi.org/10.1520/E0008_E0008M-16A.

Barrett, R. A., O'Donoghue, P. E., Leen, S. B., 2017. A physically-based constitutive model for high temperature microstructural degradation under cyclic deformation. Int. J. Fatigue 100, 388-406. https://doi.org/10.1016/j.ijfatigue.2017.03.018

Samantaray, D., Mandal, S., Bhaduri, A. K., 2009. A comparative study on Johnson Cook, modified Zerilli–Armstrong and Arrhenius-type constitutive models to predict elevated temperature flow behaviour in modified 9Cr–1Mo steel. Comp. Mater. Sci. 47(2), 568-576. https://doi.org/10.1016/j.commatsci.2009.09.025

Zhang, H., Wen, W., Cui, H., 2009. Behaviors of IC10 alloy over a wide range of strain rates and temperatures: Experiments and modeling. Mater. Sci. Eng., A 504(1-2), 99-103. https://doi.org/10.1016/j.msea.2008.10.056

Vural, M., Caro, J., 2009. Experimental analysis and constitutive modeling for the newly developed 2139-T8 alloy. Mater. Sci. Eng., A 520(1-2), 56-65. https://doi.org/10.1016/j.msea.2009.05.026

Fournier, B., Sauzay, M., Pineau, A., 2011. Micromechanical model of the high temperature cyclic behavior of 9–12% Cr martensitic steels. Int. J. Plast. 27(11), 1803-1816. https://doi.org/10.1016/j.ijplas.2011.05.007

Shankar, V., Valsan, M., Rao, K. B. S., Kannan, R., Mannan, S. L., Pathak, S. D., 2006. Low cycle fatigue behavior and microstructural evolution of modified 9Cr–1Mo ferritic steel. Mater. Sci. Eng., A 437(2), 413-422. https://doi.org/10.1016/j.msea.2006.07.146

Morito, S., Yoshida, H., Maki, T., Huang, X., 2006. Effect of block size on the strength of lath martensite in low carbon steels. Mater. Sci. Eng., A 438, 237-240. https://doi.org/10.1016/j.msea.2005.12.048

Shi, Z., Wang, M., Shi, J., Dong, H., Pu, J., Chi, B., Jian, L., 2012. Effect of tensile deformation of austenite on the morphology and strength of lath martensite. Met. Mater. Int. 18(2), 317-320. https://doi.org/10.1007/s12540-012-2015-5

Francis, J. A., Mazur, W., Bhadeshia, H. K. D. H., 2006. Review type IV cracking in ferritic power plant steels. Mater. Sci. Technol. 22(12), 1387-1395. https://doi.org/10.1179/174328406X148778

Lee, W. S., Liu, C. Y., 2006. The effects of temperature and strain rate on the dynamic flow behaviour of different steels. Mater. Sci. Eng., A 426(1-2), 101-113. https://doi.org/10.1016/j.msea.2006.03.087

Gambirasio, L., Rizzi, E., 2016. An enhanced Johnson–Cook strength model for splitting strain rate and temperature effects on lower yield stress and plastic flow. Comp. Mater. Sci. 113, 231-265. https://doi.org/10.1016/j.commatsci.2015.11.034